CHEMICAL PHYSICS

Attosecond spectroscopy of liquid water

Inga Jordan, Martin Huppert*, Dominik Rattenbacher†, Michael Peper, Denis Jelovina, Conaill Perry, Aaron von Conta, Axel Schild, Hans Jakob Wörner‡

Electronic dynamics in liquids are of fundamental importance, but time-resolved experiments have so far remained limited to the femtosecond time scale. We report the extension of attosecond spectroscopy to the liquid phase. We measured time delays of 50 to 70 attoseconds between the photoemission from liquid water and that from gaseous water at photon energies of 21.7 to 31.0 electron volts. These photoemission delays can be decomposed into a photoionization delay sensitive to the local environment and a delay originating from electron transport. In our experiments, the latter contribution is shown to be negligible. By referencing liquid water to gaseous water, we isolated the effect of solvation on the attosecond photoionization dynamics of water molecules. Our methods define an approach to separating bound and unbound electron dynamics from the structural response of the solvent.

T he study of liquid water has been at the heart of physical sciences since their emergence. Although undoubtedly the most studied liquid, water has properties that are still not entirely understood. Water displays more than 70 anomalies in its physical properties (*1–3*), such as density, heat capacity, or thermal conductivity. Even the structure of liquid water with its rapidly fluctuating hydrogen-bond network remains an object of intense debate (*4–7*). Many open questions are associated with liquid water, and their far-reaching implications explain the considerable attention that it has always attracted. A wide variety of experimental techniques have therefore been applied to its study, including nuclear magnetic resonance (*8*), infrared (IR) spectroscopy (*9*), x-ray spectroscopies (*10*), and x-ray scattering (*11*).

Despite these considerable efforts, many properties of liquid water remain mysterious. This fact is partially the consequence of a mismatch between the temporal resolution of the available techniques and the ultrafast dynamics of liquid water. A prominent example is the observation of a splitting in the x-ray emission spectrum of the outermost valence band of liquid water, which is assigned either to two structural motifs of liquid water, differing in their hydrogen-bond structure (*12*), or to dynamics in the core-hole state (*13*). Differentiation of these two interpretations would require subfemtosecond temporal resolution. Hence, probing liquid water on ever shorter time scales may allow for a better understanding of at least some of its unusual properties.

Here, we used attosecond spectroscopy to study liquid water. Whereas isolated molecules of increasing complexity have been studied with attosecond temporal resolutions (*14–17*), a deeper understanding of electronic dynamics in real chemical and biological processes requires an extension of attosecond science to the liquid phase. As the main distinguishing feature relative to most femtosecond spectroscopies, the inherent time scale of the present measurements freezes all types of structural dynamics, leaving only the fastest electronic dynamics as possible contributions.

We concentrated on the measurement of time delays in photoemission. Previous measurements on atoms (*18*, *19*) and molecules (*17*, *20*), with supporting theoretical work (*21–23*), established that such experiments access photoionization delays caused by the propagation of the photoelectron through the potential created by the parent ion. Similar measurements on metals (*24–26*) revealed the dominant influence of the electron transport time from the point of ionization to the surface. The additional role of initial-state and final-state effects was highlighted in (*27–29*). Recent work on nanoparticles (*30*) interpreted the time delays as being dominantly sensitive to inelastic scattering times on the basis of purely classical simulations that neglected the time delays due to photoionization and scattering. Here, we developed a model that describes such time delays on a fully quantum mechanical level and combined it with a semiclassical-trajectory Monte Carlo simulation of electron transport, which includes elastic and inelastic electron scattering, the quantum mechanical phase accumulated along all possible electron trajectories, and the resulting interference effects. We show that, in general, the measured time delays encode both scattering delays and mean free paths in addition to the photoemission delay.

The concept of our measurement is illustrated in Fig. 1. We used attosecond interferometry to measure the time delay between the photoemission from liquid water and that from gaseous water. Liquid water was introduced into a vacuum chamber through a quartz nozzle with an inner diameter of ~25 µm. Evaporation from the jet created the surrounding gas phase. An extreme ultraviolet (XUV) attosecond pulse train (APT), obtained through high-harmonic generation of a ~30-fs near-IR laser pulse in an argon gas cell, was focused onto the liquid microjet (spot size ~50 µm) together with a strongly attenuated replica of the IR laser pulse. This resulted in the detection of electrons from both phases simultaneously. [See (*31*) for details of the experimental setup.]

The photoelectron signals from the liquid phase were shifted and broadened relative to the gas-phase signals, which enabled their discrimination. Photoemission induced by the APT created several replicas of the photoelectron spectra (Fig. 1, blue). The simultaneous presence of the APT and IR pulses resulted in the formation of sideband spectra (Fig. 1, red). Because these sidebands can be created through two different quantum pathways, their intensity oscillates as a function of the delay between the APT and IR pulses.

A general challenge in attosecond time-resolved measurements originates from the spectral bandwidth of attosecond pulses. The resulting spectral congestion is considerably reduced by using an APT (*17*, *32*). Nonetheless, most complex systems usually have broad photoelectron spectra, which makes the application of attosecond photoelectron spectroscopy difficult. This challenge has been addressed by using metallic filters to reduce the spectral overlap (*17*, *19*) and additionally performing an energy-dependent analysis of the sideband oscillation phases (*32*, *33*). In the general case of broad overlapping photoelectron spectra, these approaches are no longer sufficient. We therefore combined these ideas with a general approach: the complex-valued principal components analysis (CVPCA) that was numerically validated in (*34*).

Figure 2 shows the experimental results obtained with APTs transmitted through Sn or Ti filters, respectively, resulting in a spectral restriction to harmonic orders 11, 13, and 15 (Sn) or 17, 19, and 21 (Ti). Shown in Fig. 2, A and B, are the photoelectron spectra recorded in the absence (blue circles) or presence (orange circles) of the IR field; Fig. 2, C and D, shows the difference spectrum ("IR on" – "IR off"; black circles) recorded on a single-shot basis by chopping the IR beam at half of the laser repetition rate. The spectra are dominated by the photoelectrons originating from the highest valence band of liquid water (light blue), the highest occupied molecular orbital (HOMO) of isolated water molecules (dark blue), and the respective sidebands (light and dark orange, respectively).

To achieve the highest accuracy, we based the analysis on principal component spectra
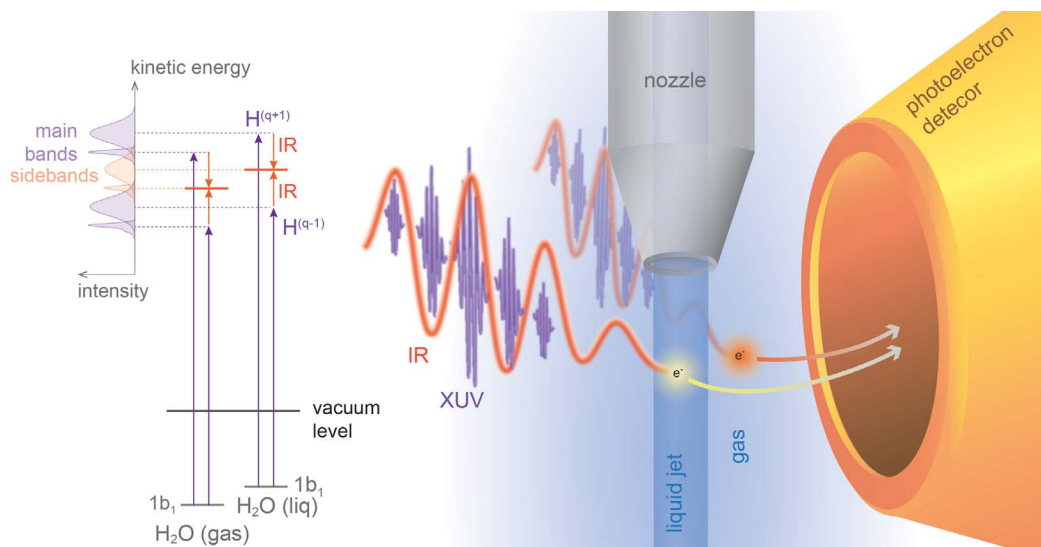
Fig. 1. Attosecond time-resolved photoelectron spectroscopy of liquid water. A spectrally filtered attosecond pulse train composed of a few high-harmonic orders (such as $H^{(q-1)}$ and $H^{(q+1)}$), superimposed with a near-IR femtosecond laser pulse, interacts with a microjet of liquid water. Photoelectrons are simultaneously emitted from the liquid and the surrounding gas phase. The resulting photoelectron spectra are measured as a function of the time delay between the overlapping pulses.

that were measured with the same liquid-microjet photoelectron spectrometer (*35*), but replacing the APT with isolated high-order harmonics selected in a time-preserving monochromator (*36*). [See (*31*) and fig. S1 for the corresponding photoelectron spectra obtained with harmonics 11 to 21.] These principal components were used to decompose the photoelectron and difference spectra in Fig. 2 into the individual contributions of the high-harmonic orders and the two phases of water. Positive contributions in the difference spectra (Fig. 2, C and D) represent sidebands, whereas the negative contributions originate from the depletion of the main photoelectron bands.

Figure 2, E and F, shows the difference spectra as a function of the APT-IR delay. Distinct oscillations with a period of 1.33 fs can be observed in both spectrograms in the spectral regions corresponding to both gas- and liquid-phase contributions. Figure 2, G and H, shows the power spectrum of the Fourier transform of Fig. 2, E and F. These images reveal the presence of the expected 2ω oscillations (where ω is the angular frequency of the IR laser).

Figure 2, I and J, shows the complex-valued Fourier transform of Fig. 2, E and F, obtained by integration over the width of the 2ω peak. Note that the phases (blue circles in Fig. 2, I and J) are not flat but vary across most energy ranges, as do the amplitudes (green triangles). We find that our CVPCA fully reproduces the complex-valued Fourier transform by attributing a unique phase shift and modulation depth to each of the principal components (*31*).

This analysis reliably provides the time delays between photoemission from the liquid and gas phases as $\Delta\tau = \tau_{liq} - \tau_{gas} = (\phi_{liq} - \phi_{gas})/2\omega$. In the case of sideband 14 (21.7 eV photon energy), we obtain $\Delta\tau = 69 \pm 20$ as; in the case of sideband 20 (31.0 eV photon energy), we

obtain $\Delta\tau = 49 \pm 16$ as. The statistical analyses leading to these results are given in table S1 and figs. S4 and S5 (*31*). The positive sign of the relative delays indicates that the electrons from liquid water appear to be emitted later than those from water vapor.

The modulation depth M, where $M = 1$ signifies a perfect contrast of the sideband oscillation, is also observable. In the gas phase, values of $M \geq 0.95$ are usually observed [see, e.g., figures 1 and 2 of (*17*) for an experiment using the same apparatus and nearly identical experimental conditions]. In the gas phase, deviations of M from unity are caused by the incoherent superposition of oscillations with different phase shifts, experimental imperfections, and/or small differences in the amplitudes of the two quantum paths leading to the same sideband state. Here, we concentrated on the analysis of the relative modulation depths between the liquid- and gas-phase signals, which eliminates the latter two effects. The relative modulation depths, defined as $M_r = M_{liq}/M_{gas}$, amount to 0.17 ± 0.03 and 0.45 ± 0.06 in the case of sidebands 14 and 20, respectively.

The near-field distributions around the liquid microjet were calculated with finite-element time-dependent methods (see figs. S6 and S7). The near-field distributions make a negligible contribution to the delay of $\tau_{liq} - \tau_{gas} = -5$ as. Moreover, they cause a reduction of the modulation contrast of 3% for the liquid phase and 6% for the gas phase. Both effects are opposite in trend to the measured results and are much smaller in magnitude.

Attosecond interferometry in liquids can be understood as a fully coherent combination of photoionization and electron scattering during transport to the surface of the jet (Fig. 3). Our previous analysis (*37*) has shown that such experiments can be rationalized by combining

the laser-assisted photoelectric effect (LAPE) with laser-assisted electron scattering (LAES). We distinguish "local" pathways, when the XUV and IR fields act at the same location in space, from "nonlocal" pathways where the XUV interaction (photoionization) and IR interaction (LAES) take place at different spatial positions.

For clarity we first discuss the one-dimensional case, modeling photoionization with an attractive potential and electron-water scattering with a shallower repulsive potential (Fig. 4). For sufficiently high photon energies, a single collision results in a total delay that oscillates between $\tau^{PI} + \tau^{sca}$ and $\tau^{PI} - \tau^{sca}$, where τ^{PI} and τ^{sca} are the Wigner delays for photoionization and scattering, respectively, as a function of the distance between the locations of LAPE and LAES with a spatial period $L = 4\pi/(k_{q+1} - k_{q-1})$ as shown in Fig. 4B. This oscillation is caused by the interference between local and nonlocal pathways along which the photoelectron wave packets have accumulated different amounts of phase because of their different central momenta (k_{q-1}, k_q, or k_{q+1}). In the presence of an exponential distribution of path lengths, corresponding to a given elastic mean free path (EMFP), the observed delay monotonically decays from $\tau^{PI} + \tau^{sca}$ to τ^{PI} (*37*). In the case of $n =$ IMFP/EMFP elastic collisions, where IMFP is the inelastic mean free path, the total delay decays from $\tau^{PI} + n\tau^{sca}$ to τ^{PI} about n times faster (Fig. 4C).

We hence draw the (general) conclusion that in the limit EMFP $\ll L/n$ (or IMFP $\ll L$), the classical limit is reached and the total delay is simply the sum of the photoionization and all scattering delays. In the opposite limit (EMFP $\gg L/n$, i.e., IMFP $\gg L$), the effects of the scattering delays cancel, such that the total delay becomes equal to the photoionization delay.

The MFPs of slow (≤50 eV) electrons in liquid water are extremely difficult to calculate and no reliable experimental measurements exist, as summarized in (38). Therefore, we developed an approach to determine the elastic and inelastic MFPs based on first-principles electron-molecule scattering calculations to determine the differential scattering cross section (DCS) for electron scattering with liquid water (39). These DCSs are used in a trajectory Monte Carlo simulation to uniquely determine the unknown EMFPs and IMFPs, required to describe electron scattering event by event, from two recent experimental measurements (40, 41). Details of this procedure are given in (39). The EMFP amounts to 0.56 nm and the IMFP to 3.8 nm at the kinetic energy corresponding to sideband 14. At the kinetic

Fig. 2. Attosecond photoelectron spectra of liquid and gaseous water. Data were acquired with a Sn-filtered APT (left) or a Ti-filtered APT (right). (**A** and **B**) Photoelectron spectra in the absence (blue) and presence (orange) of the IR field with their principal components fit (full lines) and decomposition (filled curves). (**C** and **D**) Difference spectra (circles), principal components fit (line), and decomposition (filled curves) into sidebands (orange) and depletion (blue). (**E** and **F**) Difference spectra as a function of the APT-IR time delay. (**G** and **H**) Fourier-transform power spectrum of (E) and (F). (**I** and **J**) Amplitude and phase of the 2ω component of the Fourier transform.
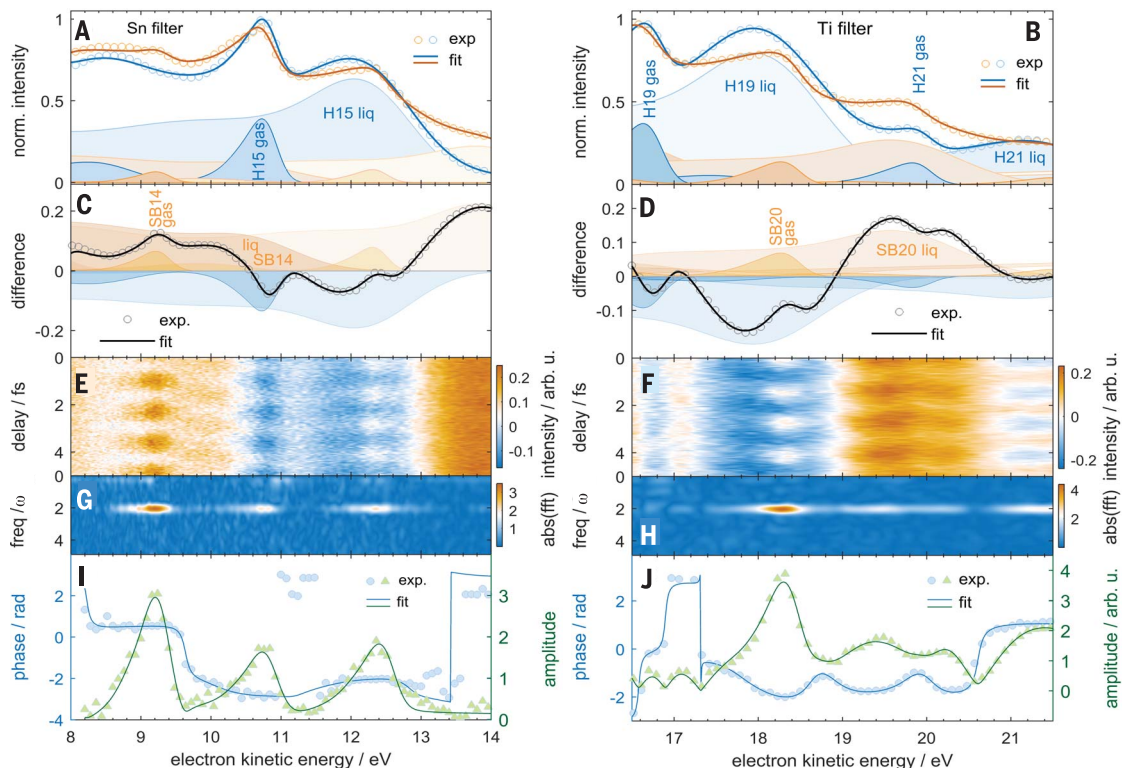

Fig. 3. Physical mechanisms of attosecond interferometry in liquid water. In the gas phase, the XUV- and IR-induced interactions are both localized to the same molecule. In the condensed phase, we distinguish "local" pathways [(1) and (2)], followed by additional scattering events without exchange of photons, from "nonlocal" pathways [(3) and (4)], consisting of ionization followed by one laser-assisted scattering event (including exchange of one photon with the IR field) among $n + n'$ non–laser-assisted collisions. Along the local pathways, photoelectron wave packets with central momenta k_q are launched. The nonlocal pathways correspond to the launch of wave packets with central momenta k_{q-1} and k_{q+1} that are converted to a central momentum k_q through a remote LAES interaction.
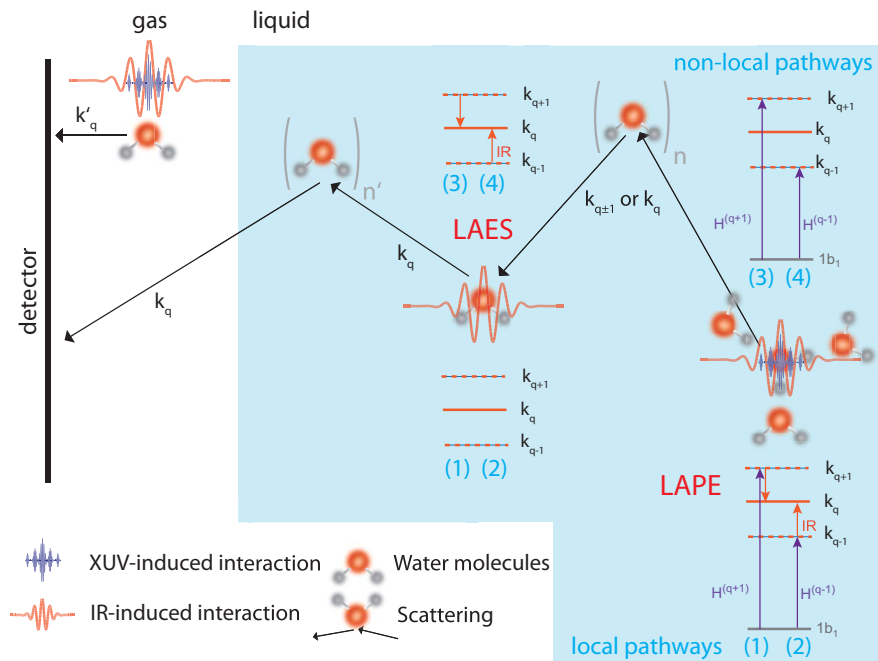
energy corresponding to sideband 20, the EMFP amounts to 0.84 nm and the IMFP to 4.6 nm. These MFPs are thus sufficiently large to cancel the scattering contributions to the total delays (Fig. 4C). Consequently, even larger values of the MFPs will not modify our results.

We further verified this conclusion through a complete three-dimensional calculation, which is described in (*31*) and implements all physical mechanisms shown in Fig. 3. Our model is based on semiclassical Monte Carlo trajectory calculations, but includes the phases and amplitudes derived from a quantum mechanical treatment of photoionization, electron scattering, LAPE, LAES, and transport in three dimensions, which were derived from our earlier one-dimensional model (*37*). The Monte Carlo trajectory calculations rely on accurate complex-valued scattering factors obtained from ab initio scattering calculations of electrons with water clusters of increasing size, and they use the associated values of the EMFP and IMFP (*39*). More than 10^8 classical trajectories were launched from at least 10^3 randomly selected initial positions with a momentum of either k_{q-1} or k_{q+1} (where $q = 14$ or 20 is realized in different sets of calculations). The results of these calculations are given in fig. S11. The contribution of electron scattering during transport amounts to 0 to 6 as, depending on the depth from which the electrons originate, which averages to ~2 as over all probed depths. Hence, these contributions are negligible in comparison to the measured delays of ~50 to 70 as.

Having excluded the contributions from electron scattering and the near-field distributions, we now turn to the photoionization delays. Figure 5 shows the calculated photoionization delays of the isolated water molecule, a water pentamer, corresponding to one complete solvation shell and a $(H_2O)_{11}$ cluster, which possesses a partial second solvation shell (*31*). A tetrahedral coordination of each water molecule with an O-O distance of 2.75 Å, corresponding to the averaged structure of liquid water, was chosen. The delays systematically increase with the addition of the first solvation shells. The increase of the delay from H_2O to $(H_2O)_{11}$ amounts to 61 as at 21.7 eV and 30 as at 31.0 eV. These numbers compare well with the experimentally measured relative delays of 69 ± 20 as and 49 ± 16 as (Fig. 5, red box), particularly when noticing the slower convergence of the delay with cluster size at the higher photon energy.

Because the solvation structure of liquid water is an important and still controversial topic [see, e.g., (*4–7*)], we studied the sensitivity of the delays to local structural distortions. Using the most representative solvation structures identified in x-ray absorption spectroscopy (*4, 12*), we stretched one O-O distance in the water pentamer from 2.75 Å
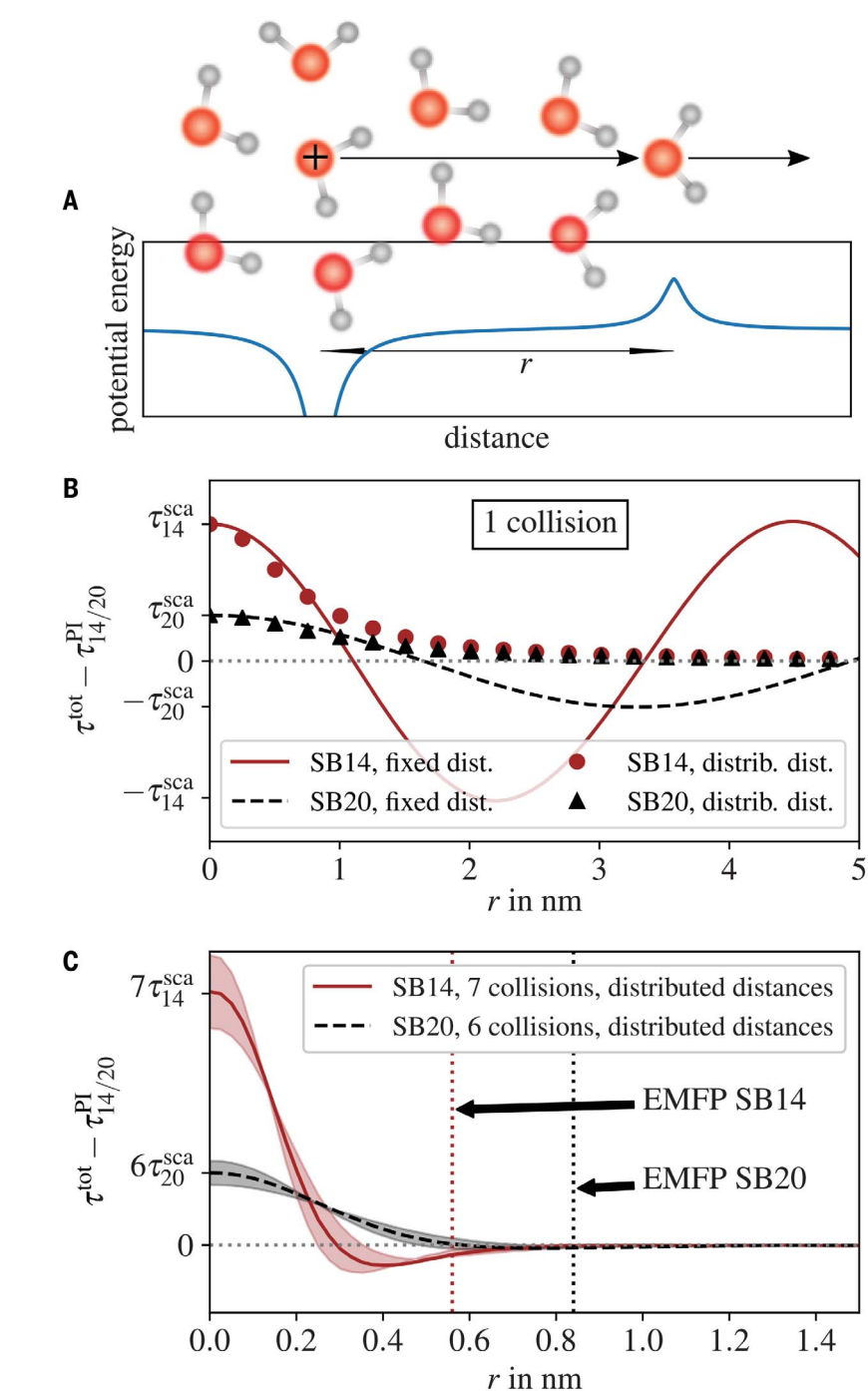

Fig. 4. Contributions of photoionization and scattering to the measured delays. (**A**) Schematic representation of the potentials used in the time-dependent Schrödinger equation (TDSE) calculations. (**B**) Total delays (τ^{tot}) for the case of a single collision at a fixed distance (lines) or an exponential path-length distribution with average r (symbols). (**C**) The case of n elastic collisions, sampled according to an exponential path-length distribution with average r. The shaded areas represent one standard deviation of the corresponding MFPs.

to 3.50 Å (Fig. 5, arrow labeled "stretched") or rotated one water molecule by 50° around the central molecule. In the case of $(H_2O)_{11}$, the same operations were applied to one group of three water molecules attached to the central

one. Our measured delays are consistent with both the unperturbed tetrahedral coordination (see Fig. 5, red box) and with a single hydrogen bond being broken by stretching (Fig. 5, dashed red box), but not by bending. Photoionization
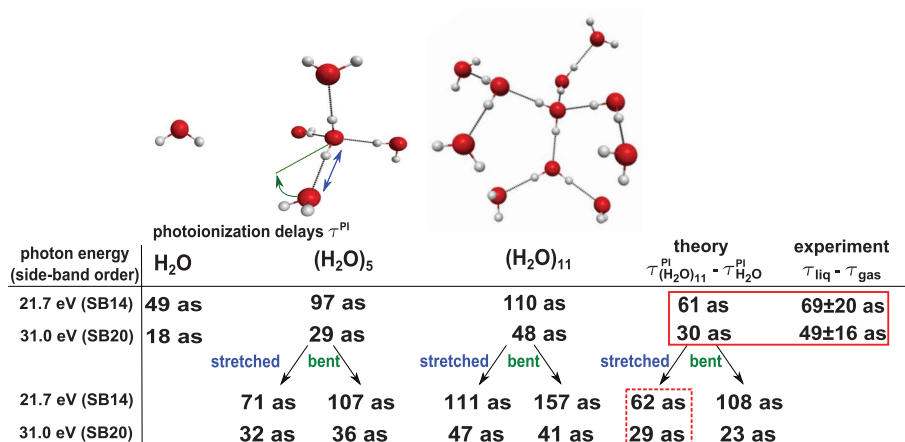
Fig. 5. Effect of the local solvation structure on photoionization delays. Calculated photoionization delays for H_2O, $(H_2O)_5$, and $(H_2O)_{11}$ are shown. The bottom two rows indicate delays obtained by stretching (arrow labeled "stretched") or bending (arrow labeled "bent") one hydrogen bond in the clusters. $(H_2O)_{11}$ was the largest entity for which fully converged delay calculations were possible, with a typical computational cost of 180 CPU days per calculation.

delays therefore discriminate between stretched or bent solvation structures, which yield indistinguishable x-ray absorption spectra [curves c and e of figure 3A in (4)]. Our measurements are thus consistent with a dominantly tetrahedral coordination of liquid water; they do not exclude the contribution of stretched hydrogen bonds, but they do exclude a dominant fraction of hydrogen bonds being broken by bending. Moreover, these sensitivities motivate the application of attosecond interferometry to ice and supercooled water, which are structurally more or less homogeneous than liquid water, respectively.

We now return to the interpretation of the reduced modulation depths observed for the liquid phase. According to Fig. 5, these finite contrasts most likely originate from a distribution of local solvation structures, which results in a distribution of photoionization delays. The superposition of interferometric oscillations with a distribution of phase shifts will indeed result in a reduced contrast of the interferometric oscillation. The larger sensitivity of the delays calculated at 21.7 eV (ranging from 110 to 157 as) compared to 31.0 eV (41 to 48 as) is consistent with the lower relative modulation depth of 0.17 ± 0.03 and 0.45 ± 0.06, respectively. An additional possible contribution to the reduced contrast comes from decoherence of electrons in liquid water. In the case of the nonlocal pathways (see Fig. 3), the collisions taking place between photoionization and LAES can cause decoherence of the propagating electron wave packet, which would also result in a reduced modulation contrast. Nonlocal attosecond interferometry therefore offers a possible approach to measuring the loss of electronic phase coherence during electron transport in matter.

The time delays determined in our work reflect the effect of the solvation environment on (i) the electronic structure of water molecules and (ii) the multiple scattering of the outgoing photoelectron. This assignment is confirmed by the dominant influence of the first two solvation shells (i and ii) and the decrease of the solvation-induced delays with the kinetic energy (ii). The measurement of photoemission time delays from liquids can thus be viewed as an attosecond time-resolved, fully coherent, electron scattering experiment from within. Relative to diffraction techniques based on external sources, it has the advantage of selectively probing the immediate environment of the ionized species. Relative to x-ray spectroscopy, it offers a temporal resolution reaching down to a few attoseconds. These aspects open new perspectives in solvation science, such as the measurement of the purely electronic solvent response after electronic excitation, relaxation, or large-amplitude chemical dynamics. They additionally offer the perspective of time-resolving both local and nonlocal electronic relaxations in the liquid phase, such as Auger decay, intermolecular coulombic decay (42, 43), and electron transfer–mediated decay (44).

Our work shows that, relative to the photoemission from the HOMO of the isolated molecule, photoemission from the most weakly bound valence band of liquid water is delayed by 50 to 70 as. Detailed calculations indicate that the contributions of electron transport to the measured delays are negligible and identify solvation as the main contribution to the measured delays. The measured delays are dominated by the first two solvation shells of water and are sensitive to the local solvation structure. Although demonstrated on practically

pure liquid water, our techniques are directly applicable to other liquids and solutions, thereby establishing the applicability of attosecond spectroscopy to solvated species. This development has the potential of expanding attosecond science into the realms of chemistry, materials science, and biology.

REFERENCES AND NOTES

1. F. H. Stillinger, *Science* **209**, 451–457 (1980).
2. J. R. Errington, P. G. Debenedetti, *Nature* **409**, 318–321 (2001).
3. A. Nilsson, L. G. Pettersson, *Nat. Commun.* **6**, 8998 (2015).
4. P. Wernet et al., *Science* **304**, 995–999 (2004).
5. J. D. Smith et al., *Science* **306**, 851–853 (2004).
6. G. N. I. Clark, G. L. Hura, J. Teixeira, A. K. Soper, T. Head-Gordon, *Proc. Natl. Acad. Sci. U.S.A.* **107**, 14003–14007 (2010).
7. K. Yamazoe, J. Miyawaki, H. Niwa, A. Nilsson, Y. Harada, *J. Chem. Phys.* **150**, 204201 (2019).
8. J. Ropp, C. Lawrence, T. C. Farrar, J. L. Skinner, *J. Am. Chem. Soc.* **123**, 8047–8052 (2001).
9. H. J. Bakker, J. L. Skinner, *Chem. Rev.* **110**, 1498–1517 (2010).
10. T. Fransson et al., *Chem. Rev.* **116**, 7551–7569 (2016).
11. T. Head-Gordon, G. Hura, *Chem. Rev.* **102**, 2651–2670 (2002).
12. T. Tokushima et al., *Chem. Phys. Lett.* **460**, 387–400 (2008).
13. O. Fuchs et al., *Phys. Rev. Lett.* **100**, 027801 (2008).
14. G. Sansone et al., *Nature* **465**, 763–766 (2010).
15. S. Biswas et al., *Nat. Phys.* **16**, 778–783 (2020).
16. P. M. Kraus et al., *Science* **350**, 790–795 (2015).
17. M. Huppert, I. Jordan, D. Baykusheva, A. von Conta, H. J. Wörner, *Phys. Rev. Lett.* **117**, 093001 (2016).
18. M. Schultze et al., *Science* **328**, 1658–1662 (2010).
19. K. Klünder et al., *Phys. Rev. Lett.* **106**, 143002 (2011).
20. V. Loriot et al., *J. Phys. Photonics* **2**, 024003 (2020).
21. J. M. Dahlström, A. L'Huillier, A. Maquet, *J. Phys. B* **45**, 183001 (2012).
22. R. Pazourek, S. Nagele, J. Burgdörfer, *Rev. Mod. Phys.* **87**, 765–802 (2015).
23. D. Baykusheva, H. J. Wörner, *J. Chem. Phys.* **146**, 124306 (2017).
24. A. L. Cavalieri et al., *Nature* **449**, 1029–1032 (2007).
25. S. Neppl et al., *Nature* **517**, 342–346 (2015).
26. M. Ossiander et al., *Nature* **561**, 374–377 (2018).
27. R. Locher et al., *Optica* **2**, 405 (2015).
28. Z. Tao et al., *Science* **353**, 62–67 (2016).
29. F. Siek et al., *Science* **357**, 1274–1277 (2017).
30. L. Seiffert et al., *Nat. Phys.* **13**, 766–770 (2017).
31. See supplementary materials.
32. M. Isinger et al., *Science* **358**, 893–896 (2017).
33. V. Gruson et al., *Science* **354**, 734–738 (2016).
34. I. Jordan, H. J. Wörner, *J. Opt.* **20**, 024013 (2018).
35. I. Jordan, M. Huppert, M. A. Brown, J. A. van Bokhoven, H. J. Wörner, *Rev. Sci. Instrum.* **86**, 123905 (2015).
36. A. von Conta, M. Huppert, H. J. Wörner, *Rev. Sci. Instrum.* **87**, 073102 (2016).
37. D. Rattenbacher, I. Jordan, A. Schild, H. J. Wörner, *Phys. Rev. A* **97**, 063415 (2018).
38. H. Shinotsuka et al., *Surf. Interface Anal.* **49**, 238–252 (2017).
39. A. Schild, M. Peper, C. Perry, D. Rattenbacher, H. J. Wörner, *J. Phys. Chem. Lett.* **11**, 1128–1134 (2020).
40. S. Thürmer et al., *Phys. Rev. Lett.* **111**, 173005 (2013).
41. Y. Suzuki, K. Nishizawa, N. Kurahashi, T. Suzuki, *Phys. Rev. E* **90**, 010302 (2014).
42. T. Jahnke et al., *Nat. Phys.* **6**, 139–142 (2010).
43. M. Mucke et al., *Nat. Phys.* **6**, 143–146 (2010).
44. I. Unger et al., *Nat. Chem.* **9**, 708–714 (2017).
45. I. Jordan et al., Data for "Attosecond Spectroscopy of Liquid Water," Zenodo (2020); http://doi.org/10.5281/zenodo.3934437.

SUPPLEMENTARY MATERIALS

science.sciencemag.org/content/369/6506/974/suppl/DC1
Materials and Methods
Figs. S1 to S12
Tables S1 and S2
References (46–59)

29 January 2020; accepted 10 July 2020
10.1126/science.abb0979

Science

Attosecond spectroscopy of liquid water

Inga Jordan, Martin Huppert, Dominik Rattenbacher, Michael Peper, Denis Jelovina, Conaill Perry, Aaron von Conta, Axel
Schild and Hans Jakob Wörner

Attosecond science in liquid phase
Many physical properties of liquid water remain unresolved due to the very fast dynamics involved in the liquid
phase. Using attosecond time-resolved photoelectron spectroscopy, Jordan *et al.* found that photoemission of electrons
from water in the liquid phase shows a time delay of about 50 to 70 attoseconds compared with photoemission from the
gas phase. This difference was attributed to solvation effects and was validated by analysis of various contributions to
the measured delays and by using theoretical simulations in water clusters of different sizes.
Science, this issue p. 974

ARTICLE TOOLS	http://science.sciencemag.org/content/369/6506/974
SUPPLEMENTARY MATERIALS	http://science.sciencemag.org/content/suppl/2020/08/19/369.6506.974.DC1
REFERENCES	This article cites 57 articles, 10 of which you can access for free http://science.sciencemag.org/content/369/6506/974#BIBL
PERMISSIONS	http://www.sciencemag.org/help/reprints-and-permissions

Use of this article is subject to the Terms of Service